X-ray measurement of a high-mass white dwarf and its spin for the intermediate polar IGR J18434-0508

Julian Gerber, Jeremy Hare, John A Tomsick, Benjamin M Coughenour, Aarran W Shaw, Maïca Clavel, Francesca Fornasini, Jules Halpern, Alyson Joens, Roman Krivonos, et al.

Monthly Notices of the ROYAL ASTRONOMICAL SOCIETY

MNRAS **530,** 861–869 (2024) https://doi.org/10.1093/mnras/stae896
Advance Access publication 2024 March 29

X-ray measurement of a high-mass white dwarf and its spin for the intermediate polar IGR J18434−0508

Julian Gerber [1]★ Jeremy Hare,[2,3,4] John A. Tomsick,[5] Benjamin M. Coughenour [5,6] Aarran W. Shaw [7] Maïca Clavel,[8] Francesca Fornasini [9] Jules Halpern,[1] Alyson Joens,[5] Roman Krivonos[10] and Koji Mukai [11]

[1]*Columbia Astrophysics Laboratory, Columbia University, New York, NY 10027, USA*
[2]*NASA Goddard Space Flight Center, Greenbelt, MD 20771, USA*
[3]*Center for Research and Exploration in Space Science and Technology, NASA/GSFC, Greenbelt, Maryland 20771, USA*
[4]*The Catholic University of America, 620 Michigan Avenue, N.E. Washington, DC 20064, USA*
[5]*Space Sciences Laboratory, University of California, 7 Gauss Way, Berkeley, CA 94720-7450, USA*
[6]*Department of Physics, Utah Valley University, 800 W. University Parkway, MS 179, Orem, UT 85048, USA*
[7]*Department of Physics and Astronomy, Butler University, 4600 Sunset Ave, Indianapolis, IN 46208, USA*
[8]*CNRS, IPAG, Univ. Grenoble Alpes, F-8000 Grenoble, France*
[9]*Stonehill College, 320 Washington Street, Easton, MA 02357, USA*
[10]*Space Research Institute, Russian Academy of Sciences, Profsoyuznaya 84/32, 117997 Moscow, Russia*
[11]*CRESST and X-ray Astrophysics Laboratory, NASA Goddard Space Flight Center, Greenbelt, MD 20771, USA*

Accepted 2024 March 26. Received 2024 February 29; in original form 2023 October 29

ABSTRACT

IGR J18434−0508 is a Galactic Intermediate Polar (IP) type Cataclysmic Variable (CV) previously classified through optical spectroscopy. The source is already known to have a hard *Chandra* spectrum. In this paper, we have used follow-up *XMM–Newton* and *NuSTAR* observations to measure the white dwarf (WD) mass and spin period. We measure a spin period of $P = 304.4 \pm 0.3$ s based on the combined MOS1, MOS2, and pn light curve. Although this is twice the optical period found previously, we interpret this value to be the true spin period of the WD. The source has an 8 ± 2 per cent pulsed fraction in the 0.5–10 keV *XMM–Newton* data and shows strong dips in the soft energy band (0.5–2 keV). The *XMM–Newton* and *NuSTAR* joint spectrum is consistent with a thermal bremsstrahlung continuum model with an additional partial covering factor, reflection, and Fe-line Gaussian components. Furthermore, we fit the joint spectrum with the post-shock region 'ipolar' model which indicates a high WD mass $\gtrsim$1.36 $M_\odot$, approaching the Chandrasekhar limit.

Key words: accretion, accretion discs – novae, cataclysmic variables – white dwarfs.

1 INTRODUCTION

Since its launch in 2002, the International Gamma-Ray Astrophysics Laboratory (*INTEGRAL*) has resulted in a number of hard X-ray catalogues surveying the full sky (Bird et al. 2010, 2016) and the Galactic Plane (Krivonos et al. 2017) from 17 to 60 keV; see Krivonos et al. (2021) for a review on *INTEGRAL*'s survey. The most recent such survey, Krivonos et al. (2022), is a catalogue of 929 'IGR' sources detected across 17 yr of *INTEGRAL* observations. While most of these sources have been identified as either active galactic nuclei (AGNs), X-ray binaries, or cataclysmic variables (CVs), there are over 100 sources yet to be classified. The strategy to classify these sources involves first finding a soft X-ray counterpart to the IGR source, which helps to localize the source better than the few arcminutes accuracy of *INTEGRAL*. With better positional accuracy, follow-up observations may be taken to classify the source. For example, this strategy was employed to identify IGR J18007−4146, IGR J14091−6108, IGR J15038−6021, and IGR J17528−2022 as Intermediate Polars by Coughenour et al. (2022), Tomsick et al. (2016), Tomsick et al. (2023), and Hare et al. (2021), respectively.

CVs are binary systems containing a white dwarf (WD) accreting from a main-sequence companion star. Intermediate Polars (IPs) are a class of CVs (magnetic CVs, or mCVs, in particular) in which the magnetic field of the WD truncates the accretion disc surrounding it. This causes the material to funnel along the magnetic field lines of the WD towards its magnetic poles. Polars are mCVs which have even stronger magnetic fields, such that no accretion disc forms around the WD at all. CVs, which accrete via Roche-lobe overflow, are copious emitters of X-rays which make them good targets to study with hard X-ray observatories such as *INTEGRAL* (Mukai 2017; Lutovinov et al. 2020).

IGR J18434−0508 (hereafter, IGR J18434) was detected in the 14-yr *INTEGRAL* hard X-ray survey of the Galaxy at RA = 280.855°, Dec. = −5.138° (Krivonos et al. 2017) A counterpart search was conducted by Krivonos et al. (2017) within the source's 90 per cent confidence error circle. Both hard and soft X-ray counterparts were found using *Swift*/BAT and *Swift*/XRT. These counterparts are 4PBC J1842.8−0506 and Swift J184311.0−050539, respectively.

★ E-mail: julian.gerber@columbia.edu

Table 1. Details of observations of IGR J18434.

Observatory	ObsID	Instrument	Start time (UT)	End time (UT)	Exposure (ks)
XMM–Newton	0890620201	MOS1	2022 March 12, 16:57:00	2022 March 13, 00:20:00	25.7
,,	,,	MOS2	,,	,,	26.0
,,	,,	pn	,,	,,	18.3
NuSTAR	30760002002	FPMA	2022 March 12, 15:16:09	2022 March 13, 15:16:09	40.2
,,	,,	FPMB	,,	,,	39.8

In a follow-up to the 14-yr *INTEGRAL* survey (Krivonos et al. 2017), Tomsick et al. (2021) identified unique *Chandra* counterparts to several of the new IGR sources with a high degree of confidence, and one of which was IGR J18434. The probability of a match between the *INTEGRAL* and *Chandra* sources was calculated as a function of number of counts between 2 and 10 keV and angular distance between the sources. The *Chandra* counterpart to IGR J18434 was determined to be CXOU J184311.4−050545 with a more accurate position of RA $= 18^{\rm h}43^{\rm m}11\overset{\rm s}{.}43$, Dec. $= -05^{\circ}05'45\overset{''}{.}2$. The sub-arcsecond *Chandra* positional accuracy allowed Tomsick et al. (2021) to also find a *Gaia* and UKIDSS counterpart to IGR J18434 using the *Gaia* EDR3 Catalogue and the UKIRT Infrared Deep Sky Survey in the VizieR database (Lucas et al. 2008; Gaia Collaboration 2021). The *Gaia* counterpart to IGR J18434 has a distance of $3.0^{+1.2}_{-0.9}$ kpc (Bailer-Jones et al. 2021) which corresponds to a 2–10 keV luminosity of $4.2^{+3.4}_{-2.6} \times 10^{33}$ erg s^{-1} (Tomsick et al. 2021). The hardness of the *Chandra* spectrum that was extracted (with a power-law photon index of $\Gamma = 0.7 \pm 0.3$) indicated that IGR J18434 was either a mCV or a high mass X-ray binary (HMXB). Using the *J*, *H*, and *K* magnitudes of the UKIDSS counterpart (UKIDSS J184311.43−050545.6) as well as the stellar colour tables in Pecaut & Mamajek (2013), it was found that IGR J18434 contained a late-type donor star, eliminating the possibility of an HMXB. It was therefore concluded by Tomsick et al. (2021) that IGR J18434 was a strong mCV candidate. In the most recent study discussing IGR J18434, Halpern & Thorstensen (2022) conducted optical spectroscopy and confirmed that IGR J18434 is a CV based on its broad Hα emission line. In that same work, time-series photometry found a period of 152.49 ± 0.02 s.

The primary new information we report in this paper is timing and spectral analysis of IGR J18434 using *XMM–Newton* and *NuSTAR*, which we use to determine the mass of the white dwarf in the CV and its true spin period. In Section 2, we describe the *XMM–Newton* and *NuSTAR* observations taken of IGR J18434 as well as the data reduction. In Section 3, we discuss the X-ray timing analysis of IGR J18434 which found a period consistent with twice the optical period. In Section 4, we discuss the spectral analysis results which established the high mass nature of IGR J18434. Finally, in Section 5, we discuss the source identification process for IGR J18434 and conclude that it is a high mass Intermediate Polar.

2 OBSERVATIONS AND DATA REDUCTION

Observations of IGR J18434 were conducted using *NuSTAR* and *XMM–Newton*. The observations were taken simultaneously, beginning on 2022 March 12. Details on these observations are listed in Table 1.

2.1 *XMM–Newton*

We reduced the EPIC/pn and EPIC/MOS data using the *XMM–Newton* Science Analysis Software (SAS v20.0). We first ran the SAS `emchain` and `epchain` scripts to generate the processed event lists for MOS and pn. For pn, we then filtered the event list using `evselect` based on the expression '(PATTERN <= 4)&&(PI in [200:15000])&&(FLAG == 0)'. We also filtered MOS1/2 with the expression '(PATTERN < = 12)&&(PI in [200:12000])&&#XMMEA_EM'. We further filtered the MOS event files for soft proton (SP) flares using the `mos-filter` script. The pn observation was conducted in Small Window mode and was thus not supported by `pn-filter`. We therefore extracted a pn light curve using `evselect` in order to manually filter for SP contamination. After finding no such flares in the pn light curve, we simply filtered the pn event list by the original good time interval (GTI) file produced by `epchain`. Additionally, the event arrival times for the pn, MOS1, and MOS2 detectors were corrected to the Solar system barycentre for timing analysis.

We then extracted three source spectra from a circular region of radius 30 arcsec centred at the source position for each instrument. We did the same for annular background regions with outer radii of 50 arcsec and inner radii of 32.5 arcsec. We then used `backscale` to account for the size of our extraction regions. Furthermore, we used `rmfgen` and `arfgen` to create the response matrices required for spectral fitting. Finally, we grouped the source spectra to contain a minimum signal-to-noise ratio of 5σ using `ftgrouppha`.

2.2 *NuSTAR*

The Level 1 science event files for ObsID 30 760 002 002 were reduced using NUSTARDAS v2.1.1 and CALDB 20220215. The analysis was done using HEASOFT version 6.30.1. Source and background regions were defined using the FPMA/B Level 2 event files. The source regions were both circular with radii of 49.2 arcsec (equal to 20 pixels). The backgrounds were rectangular regions offset from the source but on the same detector chip. Using these regions, we ran `nuproducts` for FPMA/B to create source and background spectra as well as response matrices. Like the *XMM–Newton* spectra, the *NuSTAR* source spectra were binned using `ftgrouppha` to have at least a 5σ signal-to-noise ratio. We also corrected the *NuSTAR* event arrival times to the Solar system barycentre.

3 X-RAY TIMING

We used the barycentre corrected times to create light curves of the source with *XMM–Newton* and *NuSTAR* (extracted from $r = 30$ and $r = 50$ arcsec circular regions, respectively). Notably, two strong dips separated by about 10 ks are observed. The source also appears to be rising out of a dip at the start of the observation. To further explore these dips, we extracted the pn light curves in soft (0.5–2 keV) and hard (2–10 keV) energy ranges (see Fig. 1). The energy resolved light curves show that the dips are much more prominent at soft energies compared to the hard energies. To search for a potential orbital period in the X-ray light curve, we calculated the Lomb–Scargle periodogram using the full, soft, and hard 500 s binned X-ray

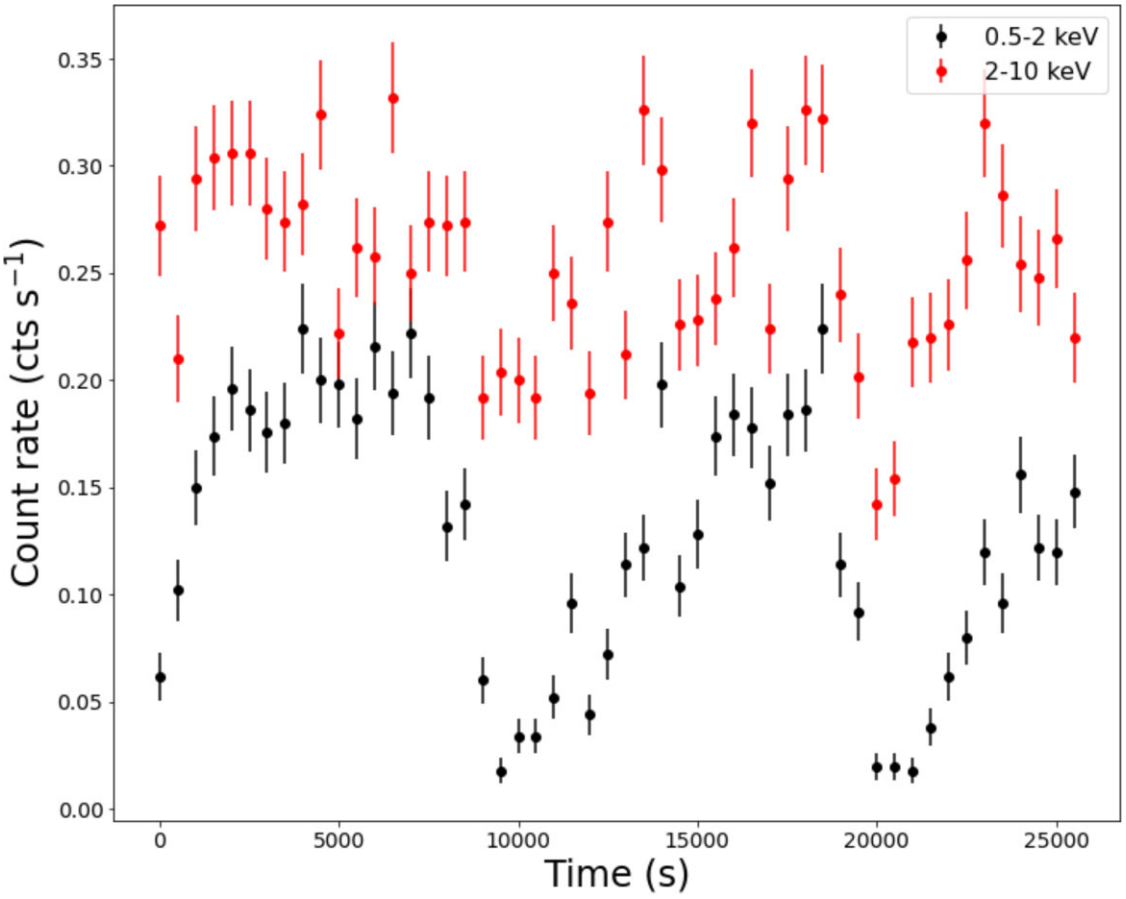

Figure 1. *XMM–Newton* EPIC pn 0.5–2 and 2–10 keV light curves with a 500 s binning. Variability is seen in both light curves, but is much more visible in the soft light curve.

light curves. A strong peak is observed around a period of about 3.1 h (however, see Section 5 for further discussion). Assuming this is the correct peak in the power spectrum, we estimate an uncertainty of 0.8 h on the period from the full width at half-max of the peak in the periodogram.

We also constructed *NuSTAR* light curves with a 1 ks binning in the full 3–79 keV energy band and the 3–10 keV energy band, since the latter overlaps with the *XMM–Newton* energy range. However, no variability is observed in either light curve. We do see evidence of variability in the 3–10 keV *XMM–Newton* light curve, suggesting that the lack of variability in the 3–10 keV *NuSTAR* light curve is due to the source having a lower signal-to-noise ratio in *NuSTAR*. It is also possible that the variability observed in the *XMM–Newton* light curve is primarily due to lower energy photons. In this case, the lack of variability in the *NuSTAR* light curve would be due to the decreased effective area of *NuSTAR* at lower energies (Harrison et al. 2013).

A periodicity of 152.49 ± 0.02 s was observed in the optical light curve of IGR J18434 (Halpern & Thorstensen 2022). We use the Z_1^2 test (Buccheri et al. 1983) to search for pulsations at this period using the *XMM–Newton* and *NuSTAR* event lists. First, we searched for the 152.49 s period using the combined (MOS1 + MOS2 + pn) event list. The largest peak found in the immediate vicinity (i.e. between $\nu = 6.47 \times 10^{-3}$ and $\nu = 6.64 \times 10^{-3}$ Hz or within $\pm 100\sigma$) of the optical period is located at 0.00657 Hz (152.3 s) but has a low $Z_1^2 = 11.1$, which is statistically insignificant after accounting for the number of trials. Expanding the search to a larger frequency range ($\nu = 0.0005$–0.01 Hz) uncovers a much stronger period ($Z_1^2 = 55.6$) at a frequency of $\nu = 0.003285 \pm 0.000003$ Hz or $P = 304.4 \pm 0.3$ s, having a False Alarm Probability (FAP) of $\sim 10^{-8}$. The results of the *XMM–Newton* Z_1^2 test are shown in Fig. 2. The uncertainties are estimated by calculating at which frequency $Z_{1,\max}^2$ falls to $Z_{1,\max}^2 - 1$. This period is about twice the observed optical period.

The 0.5–10 keV pulse profile shows only one peak per period with a relatively flat top (see Fig. 3). We calculate the pulsed fraction, defined as $(C_{\max} - C_{\min})/(C_{\max} + C_{\min})$ where $C_{\max}$ and $C_{\min}$ are the maximum and minimum number of counts in the folded pulse profile, and find a value of 8 ± 2 per cent in the 0.5–10 keV band. We also divided the *XMM–Newton* pulse profile into soft (0.5–2 keV) and hard (2–10 keV) energy bands (see Fig. 3). Interestingly, the pulse profiles are markedly different in these energy ranges, with the soft profile showing two peaks per pulse period, while the hard profile shows only one peak per period. Additionally, the peak of the hard band pulse profile falls in the minimum between the two peaks seen in the soft band pulse profile. The soft and hard bands have pulsed fractions of 15 ± 3 per cent and 10 ± 2 per cent, respectively. The observed pulsed fractions as a function of energy are plotted in Fig. 4.

We also searched for the 304.4 s period in the 3–10 keV *NuSTAR* data. However, we note that at low frequencies, the gaps in the data caused by Earth occultations due to *NuSTAR*'s low-earth orbit lead to many spurious peaks in the Z_1^2 periodogram related to the harmonics of *NuSTAR*'s orbital period. Unfortunately one of these harmonics

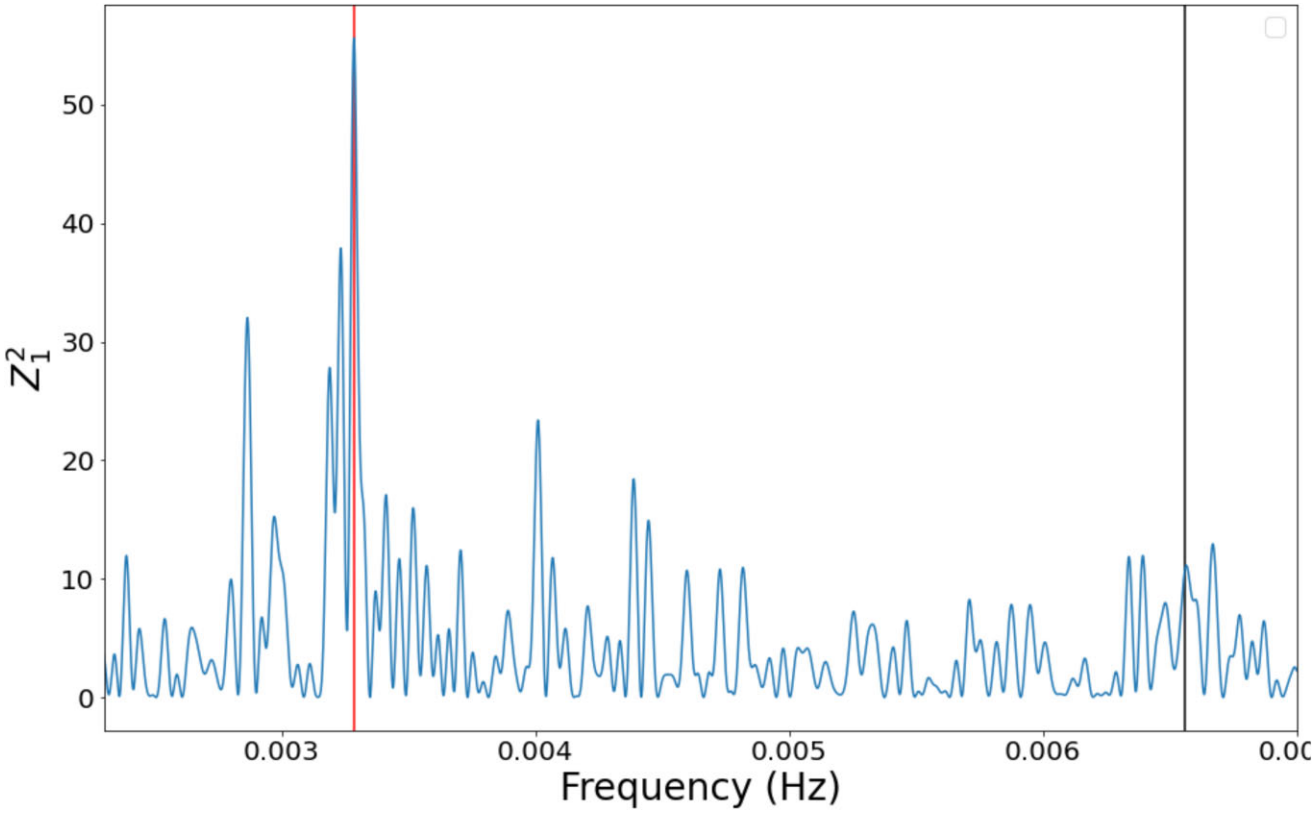

Figure 2. Z_1^2 versus frequency for the *XMM–Newton* combined MOS1, MOS2, and pn, 0.5–10 keV event list. One vertical line shows the largest peak at ∼304 s, while the other shows the location of the 152.49 s period observed in the optical power spectrum by Halpern & Thorstensen (2022).

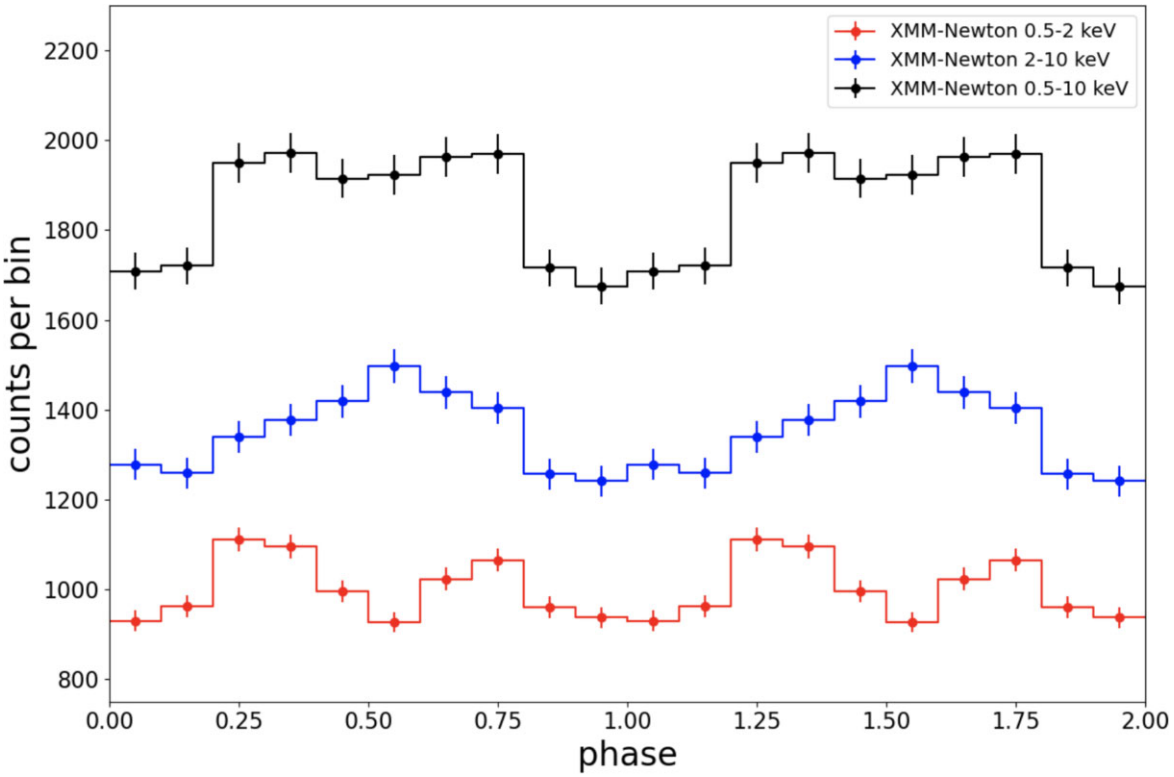

Figure 3. *XMM–Newton* combined MOS1, MOS2, and pn, 0.5–10 keV pulse profile folded on the pulse period of 304.4 s. Two phases are shown for clarity. The soft and hard band pulse profiles have an arbitrary shift applied for easier comparison between the pulse profiles.

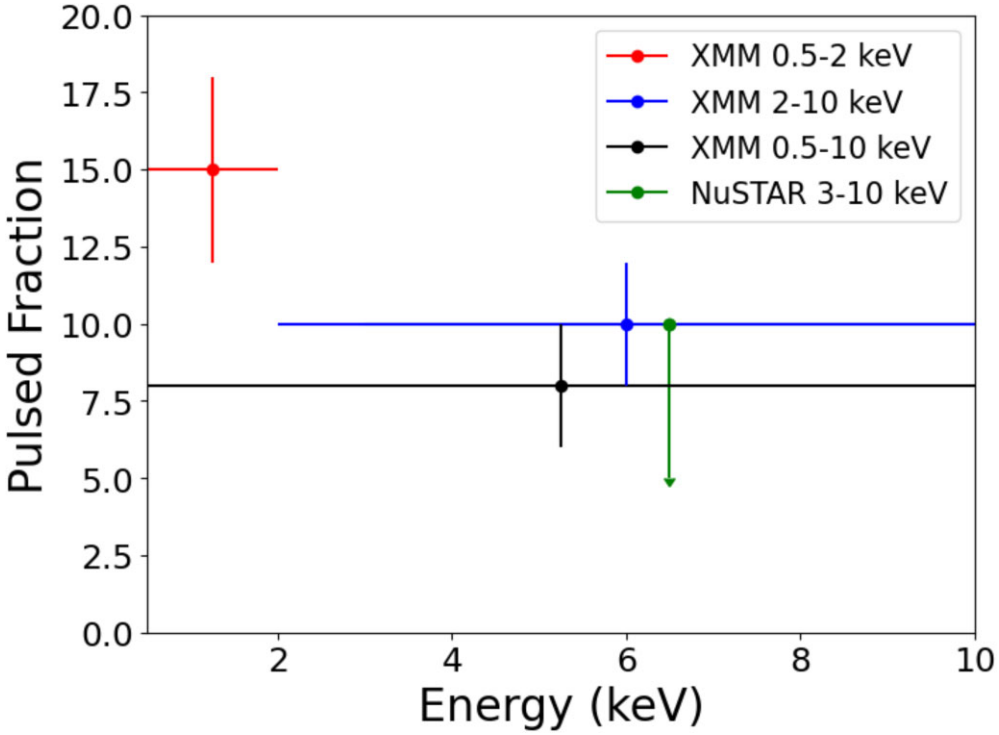

Figure 4. The measured pulsed fraction in several different energy bands. A 3σ upper-limit is provided for the *NuSTAR* non-detection.

falls very close to the pulse period, making it difficult to determine the significance of the spin period. As a secondary check, we also used the 10 s binned *NuSTAR* light curve and Stingray (Huppenkothen et al. 2019a, b) to calculate the average power spectra over continuous good time intervals longer than 3 ks, thus removing the power in the harmonics caused by *NuSTAR*'s orbit. No statistically significant peak is detected at or near the expected pulse frequency. We place a 3σ upper-limit on the observed pulsed fraction of 10 per cent in the 3–10 keV energy band.

4 X-RAY SPECTRUM

For spectral analysis, we jointly fit the *XMM–Newton* and *NuSTAR* data in the 0.5–79 keV range (0.5–12 keV for *XMM–Newton* and 3–79 keV for *NuSTAR*) using the XSPEC spectral modelling package (Arnaud 1996). In order to account for differences in normalization across instruments, we fit each spectral model using a multiplicative constant. The constant for MOS1 was frozen to 1 while the others were allowed to fit freely. Furthermore, `tbabs` was included in all fits in order to account for ISM absorption. The abundances for the `tbabs` component may be found in Wilms, Allen & McCray (2000). For all parameters listed, the errors shown are the 1σ confidence intervals.

We initially fit both a power-law and a thermal bremsstrahlung model to the IGR J18434 data. However, in both cases, the resulting $\chi^2_{\rm red}$ is unacceptably high at 2.4 and 2.5, respectively, for 820 degrees of freedom (dof). In order to improve the bremsstrahlung fit, we included the `reflect` model described in Magdziarz & Zdziarski (1995). This component modifies the model to account for reflection off of the surface of the WD. While the bremsstrahlung fit was improved by the inclusion of the `reflect` component, the resulting fit statistic ($\chi^2_{\rm red} = 1.63$ with 818 dof) was still relatively poor.

Large positive residuals below about 1 keV prompted us to include a partial covering absorption component (`pcfabs` in XSPEC). `Pcfabs` is typically included in spectral fitting of IPs (Mukai 2017). Additionally, positive residuals around 6–7 keV indicate the presence of an Fe line. A Gaussian was added to the model and freely fit to $E_{\rm line} = 6.45 \pm 0.04$ and $\sigma_{\rm line} = 0.38 \pm 0.06$ keV. This resulted in a $\chi^2_{\rm red}$ of 0.95 with 813 dof. Our best-fitting model in XSPEC was therefore `constant*pcfabs*tbabs*(gaussian + reflect* bremss)`, the best-fitting parameters of which are listed in Table 2. However, the best-fitting $\sigma_{\rm line}$ is extraneously large and thus likely includes more than one iron line. Since the $E_{\rm line}$ parameter is fitting to a value larger than 6.4 keV (the energy for a neutral iron fluorescence line), it is likely including the 6.7 keV (He-like) and 6.97 keV (H-like) lines as well. Therefore, we fit the spectrum to the same overall model, but with three separate Gaussian components. The line energy of each Gaussian was frozen to either 6.4, 6.7, or 6.97 keV, and the $\sigma_{\rm line}$ for each component was frozen to 50 eV, as was done in Coughenour et al. (2022). The best-fitting parameters for this model are listed in Table 2. The abundance parameter in the `reflect` model is the abundance of elements heavier than He relative to abundances defined in Wilms et al. (2000). The iron abundance parameter is defined in the same way and was set equal to the general abundance parameter. We froze $rel_{\rm refl}$ to 1.0 in all cases since leaving it as a free parameter resulted in values too high to be physical. The bremsstrahlung temperatures for the single and triple Gaussian fits were not significantly different at 100^{+97}_{-34} and 94.4^{+29}_{-39} keV, respectively. While the triple Gaussian fit better constrained the bremsstrahlung temperature, it is still high for an IP.

In both bremsstrahlung fits, the best-fitting abundance is lower than expected for IPs. To investigate this, we refit the data with a single Gaussian and the abundance frozen to $A = 0.5$, more in line with other IPs detected by *INTEGRAL* (Coughenour et al. 2022). The resulting fit was of similar quality to the previous fits with $\chi^2_{\rm red} = 0.96$

Table 2. Spectral results for Bremsstrahlung model fits.

Parameter[a]	Units	1 Gaussian[b]	3 Gaussians[c]
$N_{\rm H}$	10^{22} cm^{-2}	$0.17^{+0.05}_{-0.02}$	$0.17^{+0.06}_{-0.02}$
$N_{\rm H,\,pc}$	10^{22} cm^{-2}	$4.7^{+1.0}_{-0.4}$	$5.46^{+0.95}_{-1.2}$
pc fraction	–	$0.52^{+0.03}_{-0.01}$	0.53 ± 0.04
$E_{\rm line1}$	keV	6.45 ± 0.04	6.4[d]
$\sigma_{\rm line1}$	keV	0.38 ± 0.06	0.05[d]
$N_{\rm line1}$	ph cm^{-2} s^{-1}	$(2.66^{+0.23}_{-0.29}) \times 10^{-5}$	$(1.24 \pm 0.1) \times 10^{-5}$
$EW_{\rm line1}$	eV	505^{+43}_{-55}	212 ± 17
$E_{\rm line2}$	keV	–	6.7[d]
$\sigma_{\rm line2}$	keV	–	0.05[d]
$N_{\rm line2}$	ph cm^{-2} s^{-1}	–	$(0.4 \pm 0.1) \times 10^{-5}$
$EW_{\rm line2}$	eV	–	53^{+14}_{-13}
$E_{\rm line3}$	keV	–	6.97[d]
$\sigma_{\rm line3}$	keV	–	0.05[d]
$N_{\rm line3}$	ph cm^{-2} s^{-1}	–	$(0.4 \pm 0.1) \times 10^{-5}$
$EW_{\rm line3}$	eV	–	72 ± 18
$rel_{\rm refl}$	–	1.0[d]	1.0[d]
A	–	$0.007^{+0.09}_{-0.003}$	$0.006^{+0.15}_{-0.003}$
$A_{\rm Fe}$[e]	–	0.007	0.006
cos i	–	$0.75^{+0.1}_{-0.5}$	>0.28
kT	keV	100.0^{+97}_{-34}	94.4^{+29}_{-39}
$N_{\rm bremss}$	–	$(6.4^{+0.5}_{-0.2}) \times 10^{-4}$	$(6.3^{+0.4}_{-0.6}) \times 10^{-4}$
$C_{\rm MOS1}$	–	1.0[d]	1.0[d]
$C_{\rm MOS2}$	–	0.97 ± 0.02	0.97 ± 0.02
$C_{\rm pn}$	–	0.99 ± 0.02	0.99 ± 0.02
$C_{\rm FPMA}$	–	$1.19^{+0.03}_{-0.02}$	1.18 ± 0.03
$C_{\rm FPMB}$	–	1.20 ± 0.03	1.19 ± 0.03
χ^2_ν/(dof)	–	0.95(813)	0.96(813)

[a]The errors on the parameters are 1σ confidence intervals.
[c]The full XSPEC model is `constant*pcfabs*tbabs*(gaussian+gaussian+gaussian + reflect*bremss)`
[d]Frozen.
[e]Tied to parameter A.

Table 3. Spectral results for PSR model fit.

Parameter[a]	Units	PSR Model[b]
$N_{\rm H}$	10^{22} cm^{-2}	$0.20^{+0.03}_{-0.02}$
$N_{\rm H,\,pc}$	10^{22} cm^{-2}	$4.46^{+0.9}_{-0.7}$
pc fraction	–	$0.56^{+0.04}_{-0.03}$
$E_{\rm line1}$	keV	6.4[c]
$\sigma_{\rm line1}$	keV	0.05[c]
$N_{\rm line1}$	ph cm^{-2} s^{-1}	$(1.2 \pm 0.1) \times 10^{-5}$
$EW_{\rm line1}$	eV	204 ± 17
$E_{\rm line2}$	keV	6.7[c]
$\sigma_{\rm line2}$	keV	0.05[c]
$N_{\rm line2}$	ph cm^{-2} s^{-1}	$(0.38 \pm 0.1) \times 10^{-5}$
$EW_{\rm line2}$	eV	51^{+14}_{-13}
$E_{\rm line3}$	keV	6.97[c]
$\sigma_{\rm line3}$	keV	0.05[c]
$N_{\rm line3}$	ph cm^{-2} s^{-1}	$(0.36 \pm 0.1) \times 10^{-5}$
$EW_{\rm line3}$	eV	65^{+19}_{-18}
$rel_{\rm refl}$	–	1.0[c]
A	–	0.02 ± 0.01
$A_{\rm Fe}$[d]	–	0.02
cos i	–	>0.60
$M_{\rm WD}$	$M_\odot$	>1.36
$R_{\rm m}$[e]	$R_{\rm WD}$	50.2
$N_{\rm PSR}$	–	$(2.88^{+5}_{-0.2}) \times 10^{-30}$
$C_{\rm MOS1}$	–	1.0[c]
$C_{\rm MOS2}$	–	0.97 ± 0.02
$C_{\rm pn}$	–	0.99 ± 0.02
$C_{\rm FPMA}$	–	1.18 ± 0.03
$C_{\rm FPMB}$	–	1.19 ± 0.03
χ^2_ν/(dof)	–	0.96(813)

[a]The errors on the parameters are 1σ confidence intervals.
[b]The full XSPEC model is `constant*pcfabs*tbabs*cflux*(gaussian+gaussian+gaussian + reflect*atable{ipolar.fits})`
[c]Frozen.
[d]Tied to parameter A.
[e]Linked to $M_{\rm WD}$ via equations (3) and (4) in Suleimanov et al. (2016).

and 814 dof. The only parameters whose 1σ confidence intervals did not overlap with those of the original fit were the partial covering fraction ($f = 0.68 \pm 0.01$) and the bremsstrahlung normalization ($N_{\rm bremss} = 1.1 \pm 0.1 \times 10^{-3}$). Since our results are not affected by these low (and possibly unphysical) abundances, we continue to report our best-fitting results hereafter.

Next, we replace the bremsstrahlung model with the 'post-shock region' (PSR) model or 'ipolar' model from Suleimanov et al. (2016) in order to calculate the WD mass. In addition to the WD mass, this model depends on the magnetospheric radius divided by the radius of the WD, $R_m/R_{\rm WD}$. The magnetospheric radius is the point at which the accretion disc is truncated by the WD's magnetic field. By assuming that R_m is equal to the co-rotation radius of the WD, we can set $R_m = (\frac{GMP^2}{4\pi^2})^{1/3}$ where P is the spin period of the WD, which we set to 304.4 s (Suleimanov et al. 2016). $R_{\rm WD}$ can then be calculated using the well-known WD equation of state from Nauenberg (1972) relating WD mass and radius. The R_m parameter in the ipolar model can therefore be linked to the mass parameter in XSPEC according to these two equations, as was done in Tomsick et al. (2023) and Coughenour et al. (2022).

The best-fitting parameters of the ipolar fit with three Gaussians are displayed in Table 3. The spectrum and corresponding residuals are shown in Fig. 5. The best-fitting mass was 1.4 $M_\odot$, the Chandrasekhar limit and the maximum value allowed in XSPEC. This gives $R_m = 50.2$ $R_{\rm WD}$. The 1σ lower limit on the mass was 1.36 $M_\odot$. The unabsorbed flux was calculated by applying the `cflux` convolution model to the additive model components. The full model was therefore `constant*pcfabs*tbabs*cflux*(gaussian+gaussian+gaussian + reflect*atable{ipolar.fits})`. The energy range for the `cflux` component was set to 0.5–12 keV for the *XMM–Newton* spectra and 3–79 keV for the *NuSTAR* spectra. Since the cross-normalization constant factors all fit to ∼1, the best-fitting flux is applicable across instruments. The 0.5–12 keV flux is $6.36^{+0.06}_{-0.07} \times 10^{-12}$ erg s^{-1} cm^{-2}. The 3–79 keV flux is $1.43^{+0.01}_{-0.02} \times 10^{-11}$ erg s^{-1} cm^{-2}. Assuming a source distance of 3 kpc (Bailer-Jones et al. 2021), these fluxes give luminosities of $6.85 \pm 0.07 \times 10^{33}$ and $1.54^{+0.01}_{-0.02} \times 10^{34}$ erg s^{-1} in the 0.5–12 and

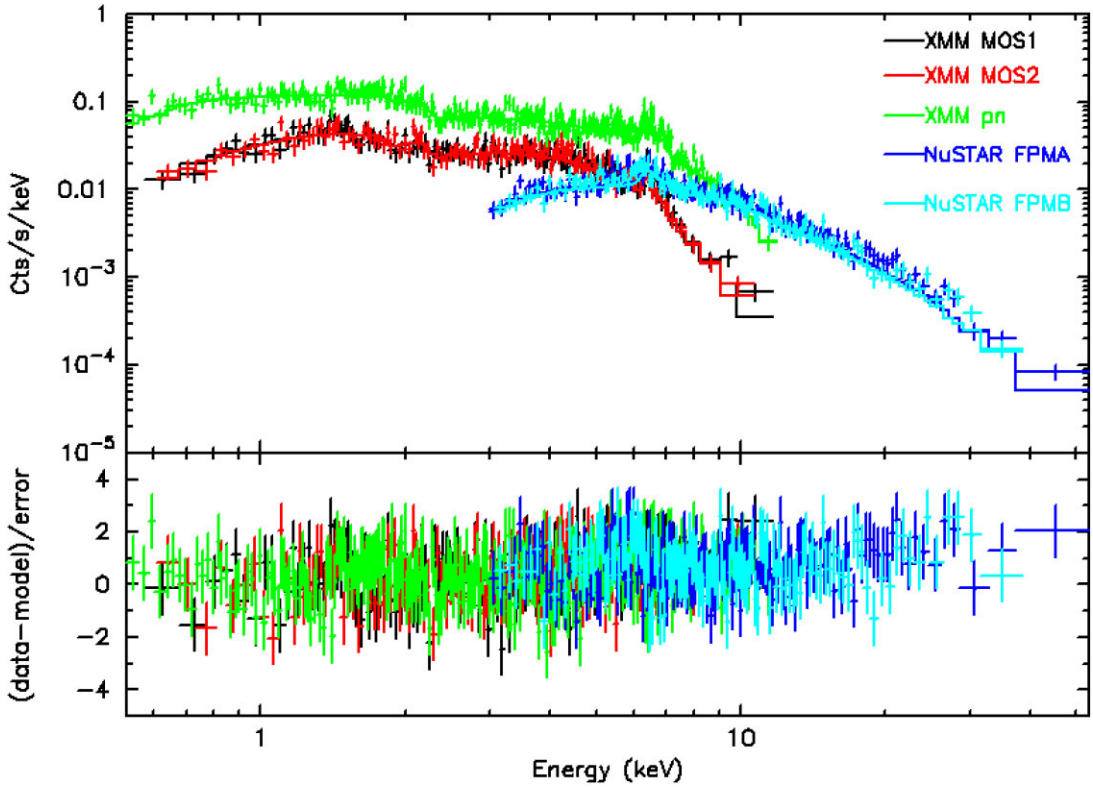

Figure 5. *XMM–Newton* and *NuSTAR* joint spectrum (with residuals) fit to the PSR model and three narrow Gaussians. The best-fitting parameters for this model are listed in Table 3.

3–79 keV bands, respectively. The flux in the 17–60 keV band is $7.0 \pm 0.1 \times 10^{-12}$ as compared to $5.2 \pm 0.8 \times 10^{-12}$ erg s^{-1} cm^{-2} reported in Tomsick et al. (2021) as measured by *INTEGRAL*.

Again, the best-fitting abundance for the ipolar fit with three Gaussians is smaller than expected. We try the same procedure as before, refitting the data with abundance frozen to $A = 0.5$. This fit gave a $\chi^2_{\rm red} = 0.98$ and 814 dof. The parameters whose 1σ confidence intervals did not overlap with those displayed in Table 3 were $N_{\rm H,pc} = 6.2 \pm 0.5 \times 10^{22}$ cm^{-2}, the partial covering fraction $=0.70 \pm 0.01$, and $\cos i = 0.3 \pm 0.1$. Although the 1σ upper limit on the mass reached 1.4 $M_\odot$, the mass was best fit to 1.36 $M_\odot$with a lower bound of 1.33 $M_\odot$.

5 DISCUSSION

The classification of IGR J18434 determined by Tomsick et al. (2021) is supported by the above spectral analysis due to its spectra being well fit to the PSR model. Furthermore, the detection of a strong iron complex in the 6–7 keV range is consistent with the X-ray properties of IPs, as is the detection of a spin period in the optical and X-ray bands.

Based on time-series photometry conducted by Halpern & Thorstensen (2022), a signal in the optical power spectrum of IGR J18434 was found at 152.49 ± 0.02 s. Through the X-ray timing analysis described in Section 3, we find a period of $P = 304.4 \pm 0.3$ s, nearly twice the previously reported signal. We therefore conclude that $P = 304.4 \pm 0.3$ s is the true WD spin period, and that the 152.49 ± 0.02 s signal is a harmonic of the fundamental period. It is fairly common for the initially discovered period to turn out to be a harmonic rather than the fundamental frequency. For example, in the case of the IP V2306 Cygni (WGA J1958.2+3232), observations from both ASCA and the Astrophysical Observatory of Catania (OACT) observed a period of about 733 s (Israel et al. 1998; Uslenghi et al. 2000). However, OACT also observed a peak in the periodograms at 1466 s, twice the previously noted period.

Norton et al. (1999) describe how two-pole accretion does not exclusively lead to a double-peaked pulse profile. Instead, two-pole accretion may lead to either a single or double-peaked pulse profile, depending on the strength of the white dwarf's magnetic field. If the magnetic field is weak, material travels along the field lines beginning closer to the surface of the WD. This produces a larger accretion region, and thus the optical depth across the accretion column can be greater than the optical depth up the accretion column. Therefore, a double peaked profile will be produced since there will be a maximum in received flux at the two observing points that align with the magnetic field lines. This double peaked effect, according to Norton et al. (1999), is predominantly seen in IPs with a WD spin period less than ∼700 s, as is the case for IGR J18434. The idea that the accretion disc is truncated close to the WD surface seems to contradict our finding that $R_m = 50.2\ R_{\rm WD}$. However, given how massive IGR J18434 is, the WD is extremely compact leading to a higher $R_m/R_{\rm WD}$. It may therefore be the case that the absolute value of R_m is more significant to the pulse profile shape than the ratio of R_m to $R_{\rm WD}$. While a double peak is observed in the 0.5–2 keV *XMM–Newton* pulse profile, only a single peak is observed in the 2–10 keV band. This difference in pulse profiles may be due to the fact that, although the geometric effects are similar at both energies, the photoelectric absorption varies.

We can use the best-fittingg R_m to estimate $\dot{M}$, the mass accretion rate and B, the surface magnetic field at the accretion region. We use the formula, $L = GM\dot{M}(\frac{1}{R} - \frac{1}{R_m})$ and $L = 1.45 \times 10^{34}$ erg s^{-1}

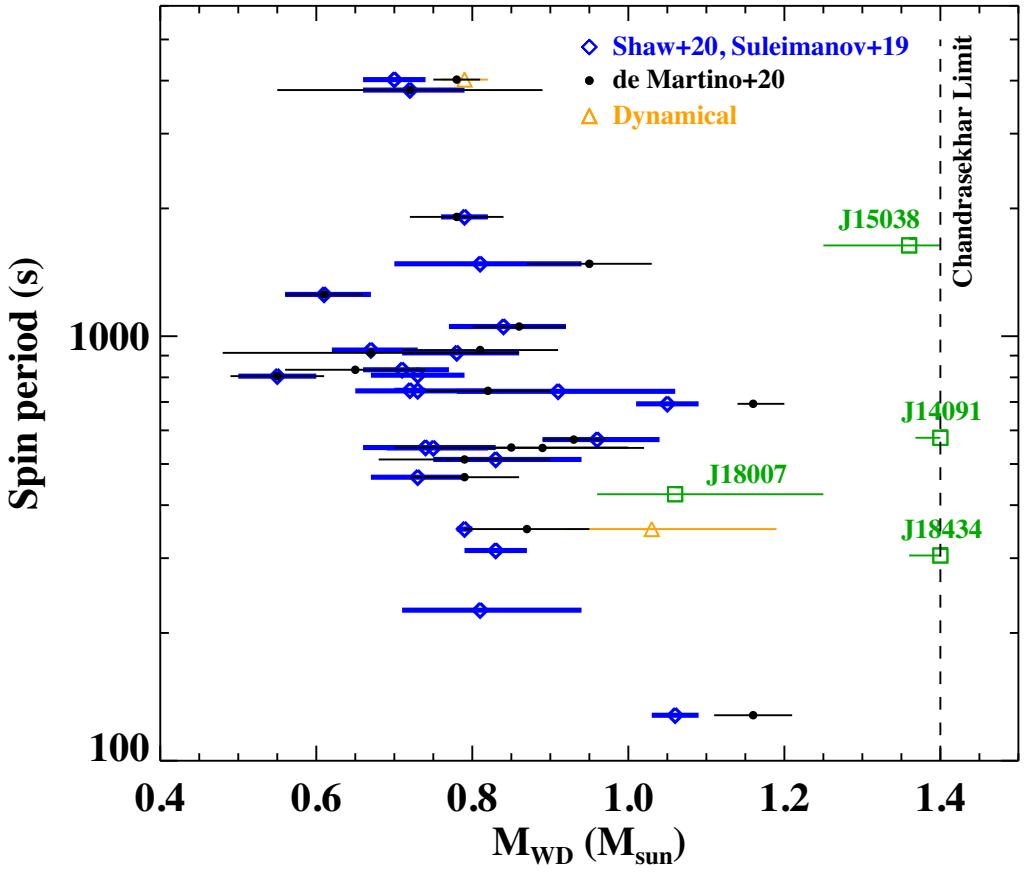

Figure 6. Plot of WD masses and spin periods of IPs. This graph is fig. 10 from Tomsick et al. (2023) with data from IGR J18434 included. The IPs marked with green squares are from our studies of IGR sources: J14091 (Tomsick et al. 2016), J18007 (Coughenour et al. 2022), J15038 (Tomsick et al. 2023), and J18434 (this work).

to find $\dot{M} = 1.3 \times 10^{16}$ g s^{-1}. We then use this value to calculate B using equation (8) in Suleimanov, Doroshenko & Werner (2019) which assumes R_m is proportional to the Alfvén radius ($R_m = \Lambda R_A$). Assuming $\Lambda = 0.5$ (as is done in Suleimanov et al. (2019)), we find $B = 94$ MG. If we use the lower bound value on the best-fitting mass ($M = 1.36$ M$_\odot$), we find $R_m = 34.9\ R_{\rm WD}$ and $B = 39$ MG. We also use equation (3) in Norton & Watson (1989) to calculate the magnetic moment, $\mu = 1.6 \times 10^{32}$ G cm^3. Here, we have assumed $\phi = 1$, or that the magnetosphere is spherically symmetric.

The estimated magnetic moment of IGR J18434, $\mu = 1.6 \times 10^{32}$ G cm^3, given $M = 1.36$ M$_\odot$, is consistent with the range of expected values (10^{32-33} G cm^3) found by Norton, Wynn & Somerscales (2004) for most IPs. Polars, in contrast, generally have higher WD magnetic moments ($\mu \gtrsim 10^{33}$ G cm^3). However, Norton et al. (2004) suggest that low magnetic moment systems (such as IGR J18434) may still evolve to polars given a long orbital period ($P_{\rm orb} > 3$ h). Follow-up observations confirming the orbital period of IGR J18434 could therefore be useful in determining its evolution.

It is possible that the 3 h peak observed in the *NuSTAR* and *XMM–Newton* light curves is the orbital period. The large modulation due to this potential orbital period is evident in the *XMM–Newton* light curves shown in Fig. 1. However, the length of the observation only spans ∼2.1 times this period, so this candidate period should be verified through additional observations. If this is the true orbital period though, it would be comparable to that of the IP BG CMi which has an orbital period of ∼3.25 h (de Martino et al. 1995). Parker, Norton & Mukai (2005) suggests that orbital modulation in IPs is due to photoelectric absorption at the accretion disc. Parker et al. (2005) predict that the inclination angle required for orbital modulation to be seen is greater than 60°. According to our spectral modelling, the angle between our line of sight and the accretion column is $\cos i > 0.60$ or $i \lesssim 50°$. There may therefore be a misalignment between the accretion column and the normal to the orbital plane. However, Mukai et al. (2015) discuss the degeneracy between the angle of the accretion column and the reflection amplitude, which makes it difficult to determine either parameter through spectral analysis alone.

The continued detection of high mass WDs by *INTEGRAL* such as IGR J14091−6108, IGR J18007−4146, and IGR J15038−6021 (Tomsick et al. 2016; Coughenour et al. 2022; Tomsick et al. 2023) may indicate that WDs in CVs gain mass throughout accretion-nova cycles. Simulations of high mass WDs ($M > 0.6$ M$_\odot$) by Starrfield et al. (2020) found that these WDs can accrete more mass than they lose via classical novae events. Once a WD gains enough mass to reach the Chandrasekhar limit (∼1.4 M$_\odot$), they may lead to Type Ia supernovae, significant for their role in cosmology as standard candles. Another possible solution to the WD mass problem is that low mass WDs in CVs lose angular momentum and merge with their donor stars, leaving a greater number of CVs with higher mass WDs to be observed (Schreiber, Zorotovic & Wijnen 2016).

Due to its high energy band, *INTEGRAL* is exceptionally well equipped to search for high mass IPs. Fig. 6 shows the WD masses

and spin periods of various IPs as measured by Shaw et al. (2020), Suleimanov et al. (2019), Ritter & Kolb (2011), de Martino et al. (2020), and our studies of IGR sources. *INTEGRAL*'s ability to detect high mass IPs is illustrated in Fig. 6 where the three IPs with masses closest to the Chandrasekhar limit are those detected by *INTEGRAL*.

ACKNOWLEDGEMENTS

JH acknowledges support from the National Aeronautics and Space Administration (NASA) under award number 80GSFC21M0002. MC acknowledges financial support from the Centre National d'Etudes Spatiales (CNES). JAT and AJ acknowledge partial support from NASA under award numbers 80NSSC21K0064 and 80NSSC22K0055.

DATA AVAILABILITY

Data used in this paper are available through NASA's HEASARC.

REFERENCES

Arnaud K. A., 1996, in Jacoby G. H., Barnes J., eds, ASP Conf. Ser. Vol. 101, Astronomical Data Analysis Software and Systems V. Astron. Soc. Pac., San Francisco, p. 17
Bailer-Jones C. A. L., Rybizki J., Fouesneau M., Demleitner M., Andrae R., 2021, AJ, 161, 147
Bird A. J. et al., 2010, ApJS, 186, 1
Bird A. J. et al., 2016, ApJS, 223, 15
Buccheri R. et al., 1983, A&A, 128, 245
Coughenour B. M., Tomsick J. A., Shaw A. W., Mukai K., Clavel M., Hare J., Krivonos R., Fornasini F. M., 2022, MNRAS, 511, 4582
de Martino D., Bernardini F., Mukai K., Falanga M., Masetti N., 2020, Adv. Space Res., 66, 1209
de Martino D., Mouchet M., Bonnet-Bidaud J. M., Vio R., Rosen S. R., Mukai K., Augusteijn T., Garlick M. A., 1995, A&A, 298, 849
Gaia Collaboration, 2021, A&A, 649, A1
Halpern J. P., Thorstensen J. R., 2022, ApJ, 924, 67
Hare J., Halpern J. P., Tomsick J. A., Thorstensen J. R., Bodaghee A., Clavel M., Krivonos R., Mori K., 2021, ApJ, 914, 85
Harrison F. A. et al., 2013, ApJ, 770, 103
Huppenkothen D. et al., 2019a, ApJ, 881, 39
Huppenkothen D. et al., 2019b, J. Open Source Softw., 4, 1393
Israel G. L., Angelini L., Campana S., Giommi P., Stella L., White N. E., 1998, MNRAS, 298, 502
Krivonos R. A. et al., 2021, New Astron. Rev., 92, 101612
Krivonos R. A., Sazonov S. Y., Kuznetsova E. A., Lutovinov A. A., Mereminskiy I. A., Tsygankov S. S., 2022, MNRAS, 510, 4796
Krivonos R. A., Tsygankov S. S., Mereminskiy I. A., Lutovinov A. A., Sazonov S. Y., Sunyaev R. A., 2017a, MNRAS, 470, 512
Lucas P. W. et al., 2008, MNRAS, 391, 136
Lutovinov A., Suleimanov V., Manuel Luna G. J., Sazonov S., de Martino D., Ducci L., Doroshenko V., Falanga M., 2020, New Astron. Rev., 91, 101547
Magdziarz P., Zdziarski A. A., 1995, MNRAS, 273, 837
Mukai K., 2017, PASP, 129, 062001
Mukai K., Rana V., Bernardini F., de Martino D., 2015, ApJ, 807, L30
Nauenberg M., 1972, ApJ, 175, 417
Norton A. J., Beardmore A. P., Allan A., Hellier C., 1999, A&A, 347, 203
Norton A. J., Watson M. G., 1989, MNRAS, 237, 715
Norton A. J., Wynn G. A., Somerscales R. V., 2004, ApJ, 614, 349
Parker T. L., Norton A. J., Mukai K., 2005, A&A, 439, 213
Pecaut M. J., Mamajek E. E., 2013, ApJS, 208, 9
Ritter H., Kolb U., 2003, A&A, 404, 301
Schreiber M. R., Zorotovic M., Wijnen T. P. G., 2016, MNRAS, 455, L16
Shaw A. W. et al., 2020, MNRAS, 498, 3457
Starrfield S., Bose M., Iliadis C., Hix W. R., Woodward C. E., Wagner R. M., 2020, ApJ, 895, 70
Suleimanov V. F., Doroshenko V., Werner K., 2019, MNRAS, 482, 3622
Suleimanov V., Doroshenko V., Ducci L., Zhukov G. V., Werner K., 2016, A&A, 591, A35
Tomsick J. A. et al., 2021, ApJ, 914, 48
Tomsick J. A. et al., 2023, MNRAS, 523, 4520
Tomsick J. A., Rahoui F., Krivonos R., Clavel M., Strader J., Chomiuk L., 2016, MNRAS, 460, 513
Uslenghi M., Bergamini P., Catalano S., Tommasi L., Treves A., 2000, A&A, 359, 639
Wilms J., Allen A., McCray R., 2000, ApJ, 542, 914

This paper has been typeset from a TEX/LATEX file prepared by the author.